Methodologies for Operando ATR-IR Spectroscopy of Magnesium Battery Electrolytes

Rudra N. Samajdar[1,2], Scott A. Brown[1,2], Shravan K. Kairy[1], Stuart D. Robertson[2], Andrew J. Wain[1]*

[1]Department of Electromagnetic and Electrochemical Technologies, National Physical Laboratory, Teddington TW11 0LW, United Kingdom

[2] WestCHEM, Department of Pure and Applied Chemistry, University of Strathclyde, 295 Cathedral Street, Glasgow G1 1XL, United Kingdom

ABSTRACT: We explore the suitability of *operando* attenuated total reflection infrared (ATR-IR) spectroscopy methodologies for the study of organoaluminate electrolytes for Mg battery applications. The "all-phenyl complex" (APC) in tetrahydrofuran (THF), with the molecular structure $[Mg_2Cl_3{\cdot}6THF]^+$ $[AlPh_4]^-$, is used as an exemplar electrolyte to compare two different spectroelectrochemical cell configurations. In one case a Pt gauze is used as a working electrode, while in the second case a thin (~10 nm) Pt film working electrode is deposited directly on the surface of the ATR crystal. Spectroscopic measurements indicate substantial differences in the ATR-IR response for the two configurations, reflecting the different spatial arrangements of the working electrode with respect to the ATR sampling volume. The relative merits and potential pitfalls associated with the two approaches are discussed.

INTRODUCTION

Magnesium batteries have been gaining interest for several years as a post-lithium ion technology for rechargeable, high energy density, electrochemical energy storage.[1-4] Mg has a higher volumetric capacity than Li, owing to the high charge density associated with its 2+ oxidation state, and is much more Earth abundant, assuaging long term concerns surrounding sustainability and security of supply. A key technological challenge impeding the commercialisation of Mg batteries lies in the development of suitable electrolytes. Simple inorganic Mg salts in conventional aprotic solvents lack sufficient ionic conductivity and metal plating/stripping kinetics, so organomagnesium chemistry has been a topic of intense study in this context.[2, 3, 5, 6] Early electrolytes comprising alkylmagnesium halide Grignard reagents (e.g. EtMgCl) were found to exhibit insufficient anodic stability but advances have been made over the last two decades, most recently via the use of magnesium organoaluminate complexes.[1, 7-9] One example that has found considerable attention is the electrolyte formed from the reaction between Grignard reagent PhMgCl and $AlCl_3$ in tetrahydrofuran (THF). The active species is believed to have the structure $[Mg_2Cl_3{\cdot}6THF]^+$ $[AlPh_4]^-$ (**Figure 1**) and so the electrolyte is commonly referred to as the "all-phenyl complex" (APC).[8, 10] We recently demonstrated that this complex can also be synthesised by a more atom-efficient reaction between Ph_2Mg and $AlCl_3$.[11]

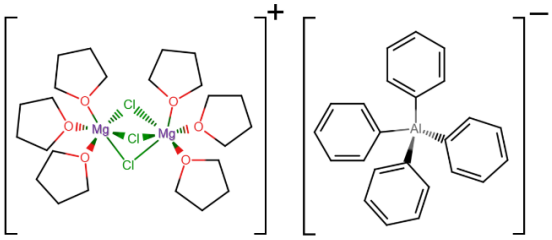

Figure 1. Structure of magnesium APC electrolyte

A critical aspect of developing new electrolytes for battery applications is understanding their interfacial behaviour under conditions of metal plating and stripping. To this end, *in situ* and *operando* vibrational spectroscopy is a powerful and well-established branch of techniques allowing the identification of chemical species and structural phases, and monitoring changes to the chemical environment associated with electrochemical processes, particularly those relevant to energy conversion and storage.[12-17]

Fourier transform infrared (FTIR) spectroscopy is particularly valuable for characterising organic solutions and so has been used in a variety of configurations for studying organomagnesium electrolytes. Aurbach *et al*. used an *in situ* grazing angle cell, in which a KBr window was coated with a thin bilayer of platinum/gold as a working electrode, to study the properties of Grignard salts, organoborane electrolytes and organohaloaluminate complexes in THF.[18] Kuwata and co-workers compared the behaviour of magnesium bis(trifluoromethylsulfonyl)imide with an organohaloaluminate-based electrolyte using an *operando* attenuated total reflection infrared (ATR-IR) configuration in which a platinum thin film working electrode is deposited directly onto a diamond ATR crystal.[19] More recently, Vizintin *et al.* developed a novel approach to *operando* ATR-IR of battery materials in which an IR transparent silicon window is fitted to the wall of a pouch cell, which is then interfaced with a germanium ATR crystal for spectroscopic analysis.[20] This method was used to characterise polyanthraquinone-based cathodes for Mg battery applications but the application was not extended to electrolytes specifically.[21-23]

An important observation emerging from the above examples is the challenge associated with understanding the spectral data acquired. At the experimental level, the range of different *in situ*/*operando* cell designs employed makes comparison between published work difficult because the configuration and geometry of the cell and sampling mode used have a major impact on what the recorded spectrum is actually measuring. As a result, it is often unclear whether spectra presented reflect changes associated with the working electrode, the electrolyte, the solid-liquid interface or a combination of these. Furthermore, difficulties in confidently assigning FTIR bands are compounded by the possibility of optical artifacts that can lead to misinterpretation. Hence, there is value in examining more

This is a peer-reviewed, accepted author manuscript of the following research article:
Samajdar, R. N., Brown, S. A., Kairy, S. K., Robertson, S. D., & Wain, A. J. (2022). Methodologies for operando ATR-IR spectroscopy of magnesium battery electrolytes. Analytical Chemistry, 94(43), 14985-14993. https://doi.org/10.1021/acs.analchem.2c02843

closely the methodological aspects of *in situ* and *operando* FTIR in the context of Mg electrolytes.

In this work we aim to highlight the importance of the above issues by comparing different cell configurations for *operando* ATR-IR spectroscopy of Mg electrolytes, using the APC/THF system as a case study. We use a spectroelectrochemical cell with a coin cell-like geometry and examine how the physical nature and location of the working electrode impact the spectra generated and the validity of their interpretation.

EXPERIMENTAL METHODS

Electrolyte Synthesis

Our APC electrolyte was synthesised using standard Schlenk techniques according to a recently published procedure.[11] In brief, Ph_2Mg was synthesised from a commercially available Grignard reagent, PhMgCl (2.0 M solution in THF, Sigma-Aldrich), to which a slight excess of dioxane was added. The Schlenk equilibrium results in a dioxane·$MgCl_2$ polymer precipitating from the solvent, leaving behind the desired product dissolved in THF, which could be easily isolated and stored under an Ar atmosphere. The Ph_2Mg was reacted with $AlCl_3$, in a 2:1 stoichiometry in THF to obtain the sole product $[Mg_2Cl_3]^+[AlPh_4]^-$. Ph_2Mg and $AlCl_3$ solutions were made up at 0.56 M and 0.28 M concentrations, respectively, so that when stirring together equal volumes of each reactant solution the final concentration of electrolyte would be 0.14 M. Higher concentrations were difficult to achieve and while 0.14 M is a relatively low electrolyte concentration for battery applications, there is only one complex in solution, the active species $[Mg_2Cl_3]^+[AlPh_4]^-$, which contains two Mg atoms per molecule; hence, the effective Mg concentration is 0.28 M.

ATR IR Spectroscopy

ATR-IR measurements were performed using a Thermo Nicolet iS50 FTIR spectrometer equipped with a liquid nitrogen-cooled mercury cadmium telluride (MCT) detector and a VeeMAX III ATR accessory (PIKE Technologies, USA) set to an incidence angle of 45°. The incident light was polarized at 90° using a built-in polarizer. Measurements were performed with a spectral resolution of 4 cm^{-1} and spectra were typically averaged over 400-500 spectral acquisitions. All ATR-IR spectra are plotted in dimensionless units of absorbance.

Operando ATR-IR measurements were performed using a modified commercial spectroelectrochemical cell (ECC-Opto-Std, EL-CELL, Hamburg, Germany), a schematic of which is presented in **Figure 2**. The ECC-Opto-Std cell body comprises a polyetheretherketone (PEEK) unit with screw fittings to allow air-tight electrode connections to be made to the working electrode and reference electrode, while a stainless steel plunger fitted with an o-ring is pushed into the PEEK body and used to contact the counter electrode. This PEEK cell body was interfaced with a 45° bevelled ZnSe ATR crystal (PIKE Technologies) via a purpose-built PEEK ATR crystal holder that is located on top of the ATR accessory. The cell body and crystal holder were compressed together using a series of screws (not shown) and a liquid-tight seal was achieved using a perfluoroelastomer o-ring (FFKM, Polymax P260, inner diameter 15.6 mm, thickness 1.78 mm). We note that the o-ring material was of critical importance in our work since compatibility with THF-based electrolytes was essential, and even minor o-ring swelling due to solvent contact compromised the seal quality.

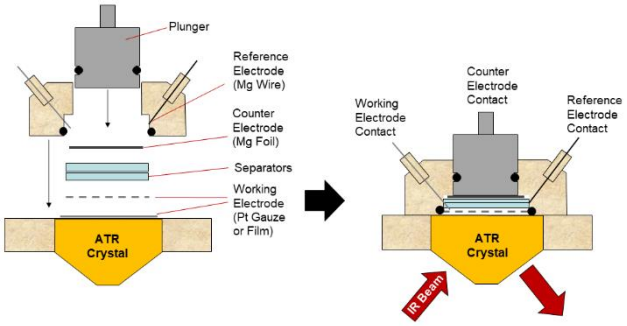

Figure 2: Schematic depiction of components and assembled cell used for *operando* ATR-IR spectroscopy. Two different configurations were employed, one using a Pt gauze and the second using a Pt film as working electrode.

The internal cell components were arranged so that a Pt working electrode (see below), was positioned in close contact with the ZnSe ATR crystal and separated from a 10 mm diameter Mg foil (Goodfellow, Cambridge, UK) disk counter electrode by two glass fibre separators (Whatman, UK), also 10 mm in diameter and approximately 0.45 mm in uncompressed thickness. The cell allows for measurements in a three-electrode arrangement, by inserting a Mg quasi-reference electrode wire (0.5 mm diameter, Goodfellow) into a dedicated reference electrode chamber in the ECC-Opto-Std cell body (see **Figure 2**). However, for simplicity, the measurements presented here were performed in a two-electrode configuration. We recognise that in this case we are strictly measuring/controlling the cell voltage and can only infer the working electrode potential with respect to the (presumed stable) redox potential established at the Mg counter electrode/electrolyte interface. However, measurements performed in the two- and three-electrode configurations showed comparable electrochemical responses, suggesting that this approach was valid.

Pt has been previously demonstrated to be a suitable working electrode in conjunction with Grignard-based Mg electrolytes,[24] so was utilised for the present study. Two different working electrode configurations were assessed: in the first case, referred to hereafter as the "Pt gauze" configuration, a Pt gauze (0.1 mm wire diameter, 0.14 mm^2 open area, Goodfellow) was placed directly on top of the ZnSe ATR crystal and used as the working electrode; In the second case, hereafter referred to as the "Pt film" configuration, a thin (~10 nm) film of Pt was sputter coated onto the surface of a clean ZnSe ATR crystal using a Quorum Q150T turbo-pumped sputter coater. The exposed working electrode surface areas were estimated at 0.99 cm^2 and 0.79 cm^2 for the Pt gauze and Pt film, respectively. In both cases electrical connection was achieved using a stainless steel pin inserted into the cell body via a screw-fitted port.

Cell assembly was performed in an Ar-filled glove box (mBRAUN LABMASTER Pro SP with O_2 and H_2O levels <0.1 ppm), after components were cleaned by ultrasonication in isopropyl alcohol and dried in a vacuum oven at 60 °C. After the solid components were assembled and an air-tight seal achieved, the cell was taken out of the glove box and located on the ATR accessory in order to record a background ATR-IR spectrum in the absence of electrolyte. Due to the ingress of moisture and CO_2 into the ATR accessory during the placement of the cell, the system was allowed to equilibrate under a flow of dry CO_2-free air provided by a purge gas generator (PG-28L,

Peak Scientific, Inchinnan, UK), for at least 30 min. After collection of the background spectrum, the cell was returned to the glove box and filled with electrolyte (<200 µL) using a glass syringe and PEEK tube connected to one of the electrode connector ports. After re-sealing the filled cell, it was allowed to equilibrate for approximately 30 min before being removed from the glove box and re-located on the ATR accessory for *operando* measurements. Prior to any potentiodynamic measurements, the assembled cell was allowed to equilibrate for a further 30 min, whilst the open circuit potential (OCP) of the cell was measured. All electrochemical measurements were performed using a CHI 600C potentiostat (CH Instruments, Austin, USA). Periodic ATR-IR measurements were also performed during this time to provide an initial spectrum of the electrolyte.

Operando ATR-IR measurements were performed by potentiodynamic cycling at 0.67 mV s^{-1}, typically in the potential range -0.8 V to 2.1 V, beginning at the OCP. This scan rate was employed to facilitate synchronisation with ATR-IR spectral acquisition, which was performed continuously whilst cycling the cell, with a potential interval of 200 mV between spectra. Since the spectral changes were very small compared to the initial spectrum recorded, *operando* spectra are presented as difference spectra, referenced against the initial spectrum measured at the beginning of the relevant cycle, unless stated otherwise. Repeat measurements were performed for each of the conditions tested and the spectra and electrochemical data shown are representative of the responses observed.

Elemental Analysis

To determine the chemical composition of plated Mg, energy-dispersive X-ray (EDX) spectroscopy was performed using a Carl Zeiss Supra™ 40 FEG Scanning electron microscope (SEM) equipped with an Oxford Instruments X-Max 50 EDX detector. An acceleration voltage of 20 kV was employed, and spectra and maps were analysed using the INCA software package. Mg plating was achieved by performing 5 potentiodynamic cycles on a Pt gauze in the *operando* ATR-IR cell between -0.8 V and 2.1 V and terminating the scan at -0.8 V. The Pt gauze was then removed by disassembling the cycled cell in the glove box, and gently rinsed with THF to remove excess electrolyte. Subsequently, the Pt gauze was quickly transferred to the SEM vacuum chamber for the analysis.

RESULTS AND DISCUSSION

In situ ATR-IR measurements at OCP

In this work we explore the application of *operando* ATR-IR to studying Mg electrolytes using APC/THF as an exemplar system. We begin by comparing *in situ* ATR-IR measurements (i.e. without electrochemical cycling) performed using the Pt gauze and Pt film configurations at OCP. **Figure 3** shows the ATR-IR spectra of 0.14 M APC/THF measured using the two different configurations after equilibration at OCP, in each case referenced against the same cell in the absence of electrolyte.

For the Pt gauze configuration (**Figure 3a**) the recorded spectrum is as expected, and is comparable to the spectrum measured using the same cell in the absence of the Pt gauze (see **Figure S1**, Supporting Information), indicating that the presence of the working electrode has minimal impact on the measurement.

Table 1 summarises the prominent bands and their assignments; we note that several of the vibrational modes strictly comprise a mixture of bond motions but for simplicity we only refer to the primary bond vibration.[25-27] The most intense bands are associated with the THF solvent, and include C-H stretching bands (2973 cm^{-1} – 2850 cm^{-1}), a C-O-C stretch (1066 cm^{-1}) and a C-C-C ring stretching mode (908 cm^{-1}). Several weaker bands are observed that are attributed to the APC electrolyte and were assigned with the aid of reference spectra recorded for Ph_2Mg in THF (**Figure S1).** Relevant electrolyte bands include the aromatic C-H stretching (3045 cm^{-1} – 2981 cm^{-1}), in-plane C-H bending (1254 cm^{-1} and 1123 cm^{-1}) and out-of-plane C-H bending (729 cm^{-1} – 665 cm^{-1}) modes associated with the phenyl group of the $[AlPh_4]^-$ anion. We also note peaks at 1029 cm^{-1} and 875 cm^{-1} which can be attributed to the C-O-C stretch and C-C-C ring stretch modes respectively, of THF molecules bound to the $[Mg_2Cl_3]^+$ cation.[18] This ability to distinguish between coordinated and non-coordinated ("free") solvent molecules by the down-shifting of the associated THF vibrational frequencies is an important observation that has been reported previously by several authors[18, 19, 28] and is central to our interpretation of the *operando* data presented later.

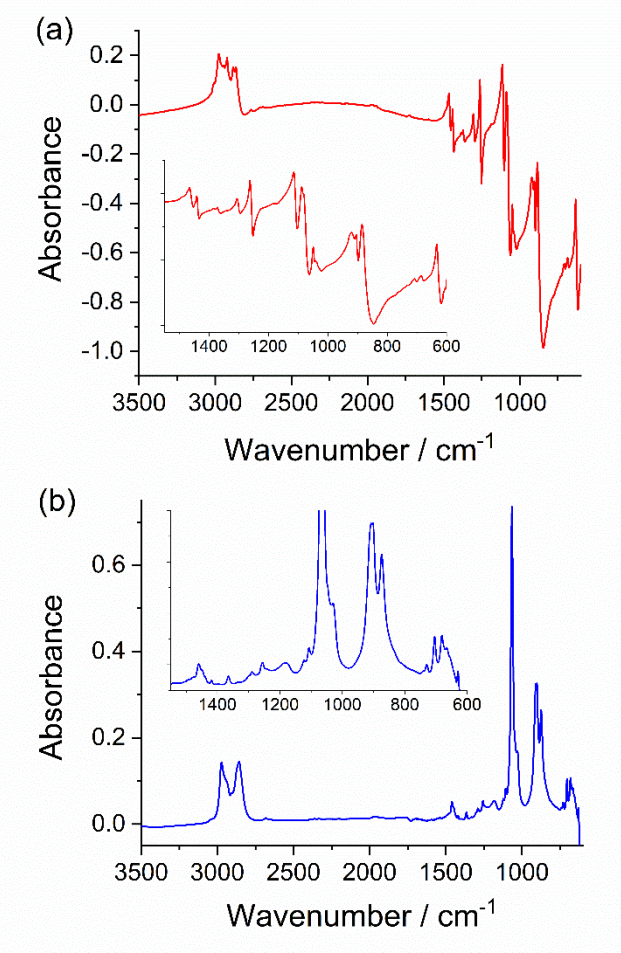

Figure 3: ATR-IR spectra of APC electrolyte-filled cell using (a) Pt gauze and (b) Pt film configurations at OCP. Spectra are referenced against the background spectrum recorded using the same cell in the absence of electrolyte.

Table 1: Summary of ATR-IR band assignments associated with pure THF, APC solutions in THF and operando ATR-IR measurements performed using APC in THF.[25-27]

Band Position / cm^{-1}				Assignment	Species
THF	APC/ THF	Operando			
		Gauze	Film		
	3045	3045	3012	C-H stretch; aromatic	$[AlPh_4]^-$
	3035	3033	2974	C-H stretch; aromatic	$[AlPh_4]^-$
	2981	2993	2946	C-H stretch; aromatic	$[AlPh_4]^-$
2973	2973	2963	2923	C-H stretch	Bulk THF
2916	2916	2941	2882	C-H stretch	Bulk THF
2850	2850	2851	2863	C-H stretch	Bulk THF
1460			1465	C-H out-of-plane deformation	Bulk THF
	1418	1418	1441	C=C stretch; aromatic	$[AlPh_4]^-$
1365	1365		1372	C-H wag	Bulk THF
		1302	1305	C-H wag/twist	Coordinated THF
1289	1289			C-H twist	Bulk THF
	1254	1258	1261	C-H in-plane deformation; aromatic	$[AlPh_4]^-$
	1123	1106	1114	C-H in-plane deformation; aromatic	$[AlPh_4]^-$
1066	1067	1067	1087	C-O-C stretch	Bulk THF
		1042	1050	C-O-C stretch	Coordinated THF
	1029	1025	1039	C-O-C stretch	Coordinated THF ($[Mg_2Cl_3]^+$)
908	909	909	916	C-C-C ring stretch	Bulk THF
		890	903	C-C-C ring stretch	Coordinated THF
	875	870	885	C-C-C ring stretch	Coordinated THF ($[Mg_2Cl_3]^+$)
	729	730		C-H out-of-plane deformation; aromatic	$[AlPh_4]^-$
	705	705	709	C-H out-of-plane deformation; aromatic	$[AlPh_4]^-$
	681	680	687	C-H out-of-plane deformation; aromatic	$[AlPh_4]^-$
	666	665	633	C-H out-of-plane deformation; aromatic	$[AlPh_4]^-$

The spectrum measured using the Pt film configuration (**Figure 3b**) exhibits spectral features at shifted band positions compared to the Pt gauze configuration, and the bands are heavily distorted, exhibiting strongly bipolar, derivative-like line shapes and a negatively sloping baseline at low frequencies. Such anomalous optical phenomena are well-documented for metal-coated ATR-IR crystals,[29, 30] and are strongly dependent on the optical properties of the metal film. The precise origin of these artefacts is not definitive, but they have been linked to dispersion effects caused by Fano resonance: interference between a discrete phonon excitation and continuous excitation.[30-32] These distortions make interpretation of the spectrum very challenging, but there may still be value in performing *operando* ATR-IR measurements in this configuration where small spectral changes are observed and interpretation is undertaken carefully. Comparing the absorbance scales in **Figure 3a** and **b** indicates similar band intensities for the two configurations, suggesting little evidence of surface enhancement associated with the Pt film,[33] although plasmonic effects cannot be ruled out.

Electrochemistry using Pt gauze and Pt film working electrode

The electrochemical response of the APC electrolyte using the *operando* ATR-IR cells was characterised by potentiodynamic cycling in a two-electrode configuration. **Figure 4** shows the voltammetry recorded for the Pt gauze (**Figure 4a**) and Pt film (**Figure 4b**) working electrodes. In both cases a cathodic current becomes discernible during the negative potential scan at potentials below 0 V, which is attributed to Mg plating on the Pt working electrode. On the positive potential scan, an anodic stripping peak is observed between 0 and 1.2 V. In both cases the magnitude of these plating/stripping peak currents increases with cycling and the stripping peak broadens, but the current begins to plateau by cycle 4. Together these suggest an electrode conditioning process at the Pt surface during the initial cycles in which new Mg nucleation sites develop with cycling. The slightly higher plating/stripping currents observed in cycle 4 for the Pt gauze can be attributed to the higher surface area of the Pt gauze compared to the Pt film (current densities were comparable for the two configurations).We note that the cycle 1 currents are higher for the Pt film and the rate of conditioning is faster than for the Pt gauze, which may reflect the more complex mass transport regime associated with the gauze working electrode. We also note the distortions and noise associated with

the plating currents at the gauze working electrode (**Figure 3a**), which we attribute to the closing of gaps between the gauze wires as the plated Mg layer thickens, resulting in rapid changes in available surface area. Repeat experiments indicated that the extent of these distortions was variable, which is a potential drawback of the use of a gauze working electrode in this cell. Nevertheless, this non-ideal behaviour does not compromise the validity of the spectroelectrochemical analysis.

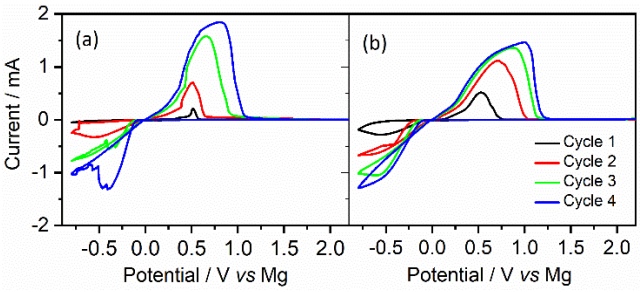

Figure 4: Potentiodynamic cycling of APC electrolyte measured using (a) Pt gauze and (b) Pt film configurations. (Cycles 1-4) Measurements were performed at 0.67 mV/s, starting at the OCP and first scanning negatively.

Measurements were also performed in a three-electrode configuration, using a Mg wire reference electrode, but comparable voltammetry to that shown in **Figure 4** was consistently observed, so for simplicity all subsequent experiments were performed using the two-electrode arrangement. Similarly, electrochemical measurements performed using the Pt gauze working electrode in a Swagelok cell yielded a similar potentiodynamic response (not shown), suggesting that the *operando* cell was able to generate suitably meaningful electrochemistry.

Operando ATR-IR measurements in the Pt gauze configuration

Operando ATR-IR data for the Pt gauze configuration are shown in **Figure 5**, in which spectra were recorded at 200 mV intervals during the potentiodynamic cycling experiment shown in **Figure 4a**. Due to the significant increase in plating/stripping currents with electrochemical cycling, we show spectra for both cycle 1 and 4. To discern the changes clearly, the presented difference spectra are referenced against the spectrum recorded at the beginning of the corresponding electrochemical cycle. Hence, bands with positive absorbance relative to the baseline reflect an increase in concentration of the associated species in the sensitive region of the ATR crystal, while bands with negative absorbance reflect a decrease in concentration.

Beginning with cycle 1 (**Figure 5a**), small but clear spectral changes are observed as the Pt electrode is initially cycled negatively from OCP (1.3 V) to -0.7 V and then positively to 2.1 V. In the negative scanning direction, weak negative bands are observed at 1067 cm^{-1} and 906 cm^{-1} both of which are associated with the bulk THF solvent. At -0.3 V a negative band is observed at 705 cm^{-1} which is assigned to the aromatic C-H bonds of $[AlPh_4]^-$ and at -0.7 V a new positive band emerges at 1043 cm^{-1} which can be attributed to coordinated THF. As the potential of the Pt gauze is scanned positively from -0.7 V, positive bands emerge at 1256 cm^{-1}, 1106 cm^{-1} and 874 cm^{-1}, all of which are associated with $[AlPh_4]^-$. At -0.1 V the coordinated THF band at 1043 cm^{-1} becomes attenuated. A subtle but important change is observed at 0.5 V, which coincides with the stripping peak for cycle 1: for this potential only, new positive bands are observed at 1022 cm^{-1} and 3045 cm^{-1}, and the previously negative band at 705 cm^{-1} becomes positive. This suggests that the stripping process leads to an instantaneous, transient increase in a solution phase organic species. This is discussed further below, but the bands described are consistent with the $[AlPh_4]^-$ anion complex (see **Figure S1**). The fact that several of the above bands are still present at the positive vertex potential of 2.1 V where no current is measured in the cell, indicates that either the changes observed during this first cycle are irreversible, or the ATR response is slow to equilibrate. We discuss the origin of these below in the context of complete cell cycles.

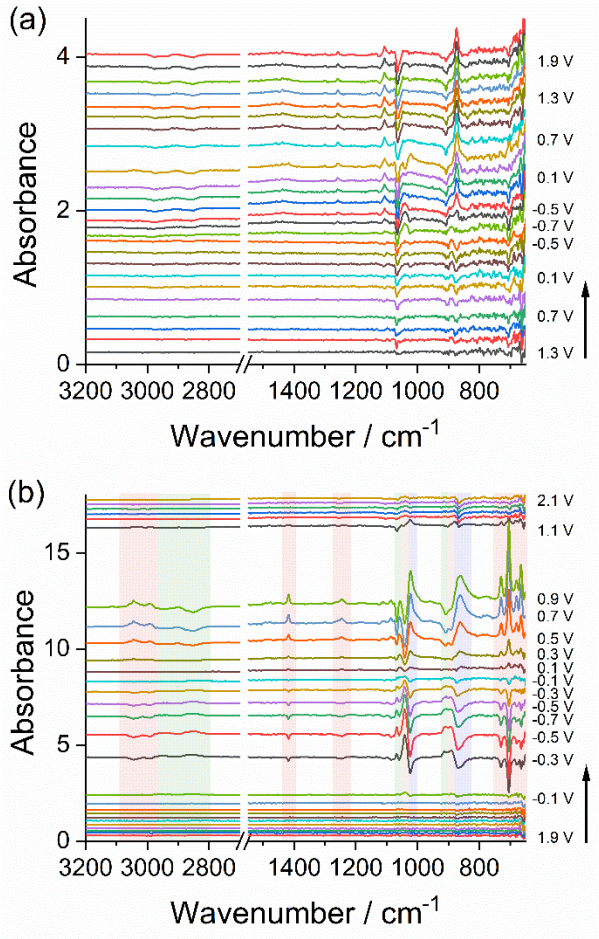

Figure 5: *Operando* ATR-IR difference spectra measured using Pt gauze configuration for (a) cycle 1, referenced against the initial spectrum at OCP and (b) cycle 4, referenced against the spectrum recorded at the beginning of this cycle (at 2.1 V). Spectra are arbitrarily offset in the vertical axis for visibility. Red boxes: $[AlPh_4]^-$, blue and yellow boxes: coordinated THF; green boxes: bulk THF.

During cycle 4 (**Figure 5b**), similar spectral changes are observed to cycle 1, albeit with notably higher band intensities, which is consistent with the higher Mg plating and stripping currents measured in the electrochemical response (**Figure 4a**). In the plating region (-0.1 V to -0.7 V) a group of four prominent negative bands is observed between 730 cm^{-1} – 660 cm^{-1}, with other weaker negative bands at 3045 cm^{-1}, 2990 cm^{-1}, 1418 cm^{-1} and 1248 cm^{-1}. These bands are all attributed to the phenyl ring of the $[AlPh_4]^-$ anion complex, consistent with the observations from cycle 1. For clarity, these bands are highlighted by

red shaded boxes in **Figure 5b**. We also observe negative bands at 1025 cm^{-1} and 870 cm^{-1} (blue boxes, **Figure 5b**) which are respectively attributed to the C-O-C stretch and C-C-C ring stretching modes of THF molecules coordinated to the $[Mg_2Cl_3]^+$ cation . Closely associated with these bands are positive bands at 1040 cm^{-1} and 890 cm^{-1} (yellow boxes, **Figure 5b**) which we assign to the C-O-C/C-C-C ring stretches of coordinated THF molecules in a new coordination environment, different to the $[Mg_2Cl_3]^+$ complex (see discussion below). Finally, positive bands (green shaded boxes, **Figure 5b**) are observed at 2960 cm^{-1}, 2850 cm^{-1}, 1067 cm^{-1} and 908 cm^{-1}, all of which can be attributed to free THF.

Importantly, as the potential is swept positively from -0.7 V there is a band attenuation followed by an intensity inversion of all bands, consistent with a reversal in the local electrolyte composition changes observed during Mg plating. We note that the band intensity begins to decrease at potentials more positive of -0.5 V, despite the stripping process not starting until above 0 V, which can be explained by the diffusive replenishment of the depleted electrolyte at the ATR crystal surface as the plating current decreases. An abrupt attenuation of the above bands is observed between 0.9 V and 1.1 V, coincident with the tail of the stripping peak in the electrochemical response (**Figure 4a**), indicating that the local solution composition has returned almost to its initial state beyond this potential. From this we can conclude that the primary changes being observed in the *operando* spectra are reversible and are intimately associated with the plating/stripping process.

Taken together, these observations are consistent with $[AlPh_4]^-$ anions from the electrolyte being displaced or consumed from the solution in the vicinity of the ATR crystal during Mg plating, and hence an apparent loss in intensity of the associated aromatic bands. This occurs with loss of coordinated THF and increase in bulk THF concentration, consistent with $[Mg_2Cl_3{\cdot}6THF]^+$ ions being consumed at the working electrode with release of THF molecules bound in this complex. The emergence of a new THF coordination environment, revealed by the THF bands at 1040 cm^{-1} and 890 cm^{-1} that are intermediate to the bulk and fully complexed THF bands, is consistent with the change in ionic composition and may also reflect the solvation of a new (e.g. Cl^- or $MgCl^+$) species produced during Mg plating.

Two possible reasons for the significant changes in $[AlPh_4]^-$ concentration during Mg plating/stripping are: (i) co-deposition of the $[AlPh_4]^-$ anions with Mg onto the platinum surface, possibly due to $[Mg_2Cl_3{\cdot}6THF]^+$ $[AlPh_4]^-$ ion pairs becoming trapped in the Mg metal deposit or the formation of crystalline electrolyte deposits, or; (ii) migration/electrostatic repulsion of the $[AlPh_4]^-$ anions away from the negatively charged working electrode resulting in a local depletion in solution within the sampling volume of the ATR crystal. We favour the latter argument because an anion concentration gradient would be expected to develop across the cell and the extent and direction of this gradient should scale with the current. However, to rule out the possibility of electrolyte anion co-deposition we performed elemental analysis using SEM/EDX on a Pt gauze electrode after potentiodynamic cycling (see **Figure S2**). These measurements indicated that the element Al was only present in very low concentrations on the surface of the Pt gauze (of the order of 1 at. %, close to the limit of detection of the instrument), suggesting that any co-deposition of Al with Mg was negligible and that Al was likely only present as a salt residue after drying.

Whilst the most significant spectral changes observed in cycle 4 appear to be reversible, as noted for cycle 1 there are some spectral features that are still visible after the cycle is complete, indicating some irreversibility on this experimental timescale. This can be seen most clearly in **Figure S3**, which shows difference spectra recorded at 1.3 V (**Figure S3a**) and -0.7 V (**Figure S3b**) for the first five complete cycles, all referenced against the same initial spectrum recorded at OCP. The most prominent changes are positive aromatic bands at 1106 cm^{-1} and 1259 cm^{-1}, both of which we attribute to $[AlPh_4]^-$, and an intense positive band at 875 cm^{-1} which we attribute to coordinated THF. We also observe negative bands at 1062 cm^{-1} and 907 cm^{-1} that are associated with bulk THF. All of these changes suggest a gradual increase in electrolyte concentration within the sampling volume of the ATR crystal with successive cycling. The reasons for this are unclear, but one explanation could be the gradual local accumulation of $[Mg_2Cl_3{\cdot}6THF]^+$ and $[AlPh_4]^-$ ions due to restricted diffusion at the interface between ATR crystal and the working electrode, leading to incomplete equilibration at this potentiodynamic scan rate. An alternative argument is the gradual loss of THF solvent, either through evaporation due to incomplete sealing or absorption into the polymeric o-rings of the cell. However, the latter was ruled out by spectroscopic measurements performed in this configuration at OCP for several hours, which showed negligible spectral changes.

Operando ATR-IR spectroscopy in the Pt film configuration

Having explored the response of the Pt gauze configuration, we next consider the Pt film configuration. **Figure 6a** shows the *operando* ATR-IR data recorded during cycle 1, in which the spectra are in stark contrast to those measured using the Pt gauze. Not only are the signal intensities larger for the Pt film by at least an order of magnitude, but asymmetric, bipolar/derivative-like line shapes are exhibited, similar to those observed for the spectrum in **Figure 3b**. Whilst caution is recommended in interpreting these spectra, the bands coincide with those observed in the OCP spectrum shown in **Figure 3b**, indicating that the bands in **Figure 6a** reflect changes in the concentration of species already present, rather than the formation of new species (which would be evidenced by the growth of bands). The most intense bands also appear to be equivalent to those observed for the Pt gauze (**Figure 5b**) although we note the higher relative absorbance intensity at higher frequencies. Comparison of band positions against the Pt gauze data (**Table 1**) indicate some band shifting resulting from the Pt-coating of the ATR crystal.

For cycle 1 (**Figure 6a**), the spectra remain relatively flat as the potential is scanned negatively from OCP (1.3 V), with substantial changes only observed at -0.7 V, where the observed THF and $[AlPh_4]^-$ bands all appear to be negative with respect to the baseline. Upon reversal of the potentiodynamic scan direction these bands intensify, but interpretation becomes more challenging as the bipolar/derivative-like line shapes become more extreme; nevertheless, the observed bands appear to be predominantly negative. The spectra then remain largely unchanged until a potential of 0.7 V is reached, coinciding with the stripping potential, at which point the spectrum resembles that measured at -0.7 V.

A notable difference here is the absence of the intensity inversion that was observed during the positive potential sweep in the case of the Pt gauze (**Figure 5b**). Above 0.7 V a series of relatively weak bands remain, suggesting a degree of irreversibility as noted for the Pt gauze configuration. In addition to the changes in individual band intensity with potential, at potentials above -0.7 V in the positive direction the baseline begins to slope considerably, with a substantial drop in broadband absorbance below 3000 cm^{-1} that becomes more extreme with decreasing frequency (**Figure 6a**). The baseline then flattens above 0.7 V. The scale of this baseline shift is sufficiently large that it is also clearly visible in the spectra referenced against the empty cell (**Figure S4**), and it very clearly coincides with the plating and stripping potentials. This sloping baseline along with the higher relative intensity of high frequency bands in the difference spectra noted above can be explained by a substantial, frequency-dependent, loss in broadband optical transparency of the Pt-coated ATR crystal surface as it becomes plated with a layer of Mg.

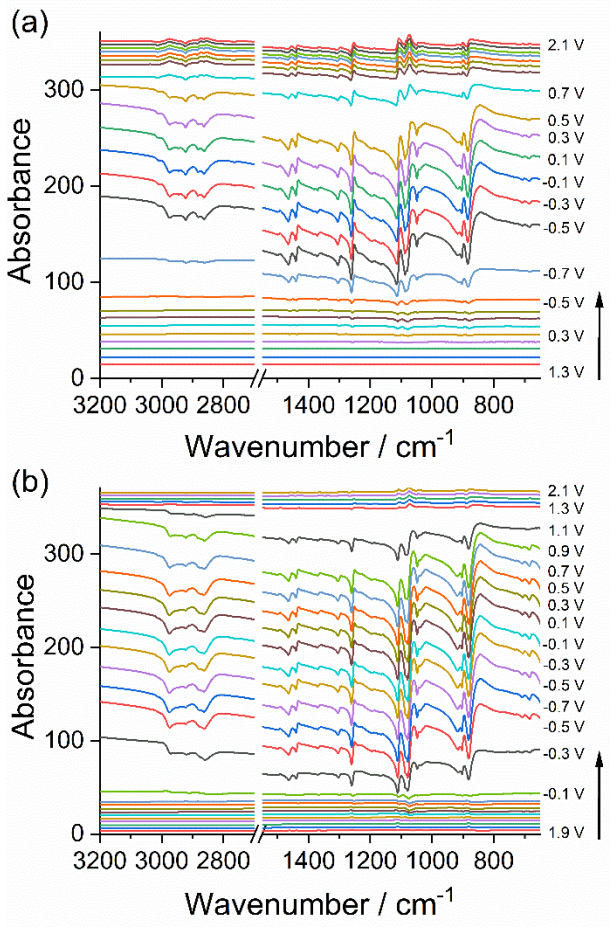

Figure 6: *Operando* ATR-IR difference spectra measured using Pt film configuration for (a) cycle 1, referenced against the initial spectrum at OCP and (b) cycle 4, referenced against the spectrum recorded at the beginning of this cycle (at 2.1 V). Spectra are arbitrarily offset in the vertical axis for visibility.

For cycle 4 (**Figure 6b**), the spectra are qualitatively similar to cycle 1 but with the notable difference that the abrupt changes observed during the negative potential scan occur earlier in the cycle, at a potential of -0.3 V, and these changes are not reversed until beyond 1.1 V on the positive potential scan. Both of these observations are consistent with the associated electrochemical response (**Figure 3b**), in which an earlier onset of plating on the negative potential scan and a broader stripping peak on the positive potential scan are observed for cycle 4 compared to cycle 1. Unlike the Pt gauze configuration, the intensity of spectral changes for cycle 1 and cycle 4 are comparable, suggesting that the Pt film configuration is more sensitive to changes taking place during the early stages of plating than the gauze and the spectral sensitivity quickly reaches saturation.

Focusing on the irreversible changes observed over successive cycling (**Figure S3c** and **S3d**), once again the bipolar/derivative-like line shapes make detailed analysis challenging, but spectral features coincide with the THF and $[AlPh_4]^-$ bands, indicative of a concentration imbalance developing across the cell, as observed for the Pt gauze (**Figure S3a and S3b**).

General Discussion

The Pt gauze and Pt film cell configurations clearly generate contrasting *operando* ATR-IR spectral responses despite the electrochemical process taking place being largely the same. The different behaviours can be understood by considering the geometry and location of the Pt working electrode with respect to the evanescent wave at the ATR crystal surface, which has an estimated penetration depth of 1.7 µm into solution (see ESI, **Section S1**). A schematic depiction illustrating the different sampling regions for these two configurations is shown in **Figure 7**.

In the case of the Pt gauze, since the direct contact area between the working electrode and the ATR crystal is comparatively very small (<5% of the total area), the sampling volume is composed largely of electrolyte solution that is local to, but not immediately adjacent to, the Pt electrode. The result is that the spectral response is dominated by changes in electrolyte solution composition in the vicinity of the Pt electrode brought about by Mg plating and stripping. These changes appear to be qualitatively the same across all cycles (including the initial cycle), albeit with increasing intensity with cycling as the plating/stripping currents increase. The primary changes with Mg plating are identified as a depletion of $[AlPh_4]^-$ anions from solution with commensurate increase in bulk THF concentration. Meanwhile, electrochemical reduction of $[Mg_2Cl_3]^+$ at the Pt surface results in a loss of coordinated THF molecules from the cation complex, causing a loss in associated band intensity. Importantly the by-products of Mg plating, which may include species such as Cl^- and $MgCl^+$.[34-36] We propose that the solvation of these species generates a new coordination environment for THF molecules close to the electrode surface and thus leads to an additional set of THF bands during plating (highlighted in yellow in Figure 5). An alternative way to understand these changes is to consider the coordinated THF bands as undergoing a shift to higher frequencies as THF molecules are released from $[Mg_2Cl_3]^+$ to a less tightly-bound solvation state.

These changes are in contrast to those observed by Aurbach *et al.* for $Mg(BPh_2Bu_2)_2$/THF electrolyte solutions for which *in situ* FTIR measurements indicated an *increase* in phenyl group band intensity with plating that the authors tentatively attributed to the adsorption of $PhMg^+$ or $BPh_2Bu_2Mg^+$ species.[18] In addition to the differing chemistry of this system from the APC electrolyte studied in our work, the likely origin of these opposing observations can be explained by the fact that our Pt gauze experiment primarily probes the local electrolyte composition, rather than the Pt electrode surface. On one hand this may be

considered a limitation of the gauze configuration, since only changes in the solution phase are detected, and the response appears to be largely insensitive to any chemistry taking place at the electrode-electrolyte interface. However, the absence of any optical artifacts introduced by the presence of the working electrode combined with the relative simplicity of spectral interpretation gives this approach some advantages.

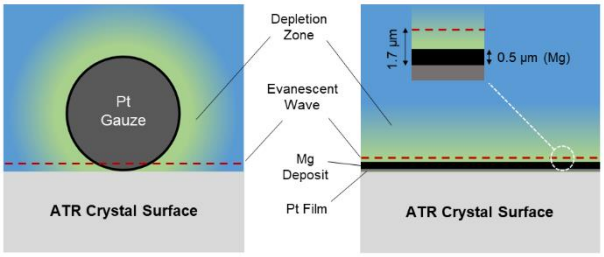

Figure 7. Schematic depiction of sensing region adjacent to ATR crystal surface for Pt gauze (left) and Pt film (right) configurations. The inset in the right hand panel shows the approximate thickness of the plated Mg layer and the penetration depth of the ATR evanescent wave. Note that the thickness of the depletion layer is expected to extend well beyond the ATR-IR sensing region. The figure is for illustrative purposes only and features are not to scale.

In the case of the Pt film, the Pt acts as an extension to the ATR crystal so the entire working electrode surface and immediately adjacent electrolyte is included in the sampling volume. Moreover, the electrode-electrolyte interface occupies the most sensitive region of the evanescent wave emerging from the ATR crystal, so the response is highly sensitive to interfacial phenomena. The key observations here are a loss of broadband absorbance together with a decrease in intensity of the measured vibrational bands during plating, both of which can be explained by the deposited Mg blocking the transmission of the incident and reflected light. We note that Kuwata and co-workers acknowledged this issue in their work using a platinum-coated diamond ATR crystal, and reported a need to restrict how thick the Mg deposit became.[19] Based on the integrated stripping current we estimate a minimum deposited Mg thickness of approximately 0.5 µm (for cycle 4, see ESI **Section S2**), which already represents a substantial fraction of the ATR penetration depth. Assuming that the density of the deposited Mg is lower than that of pure Mg metal, which is to be expected given the likely nanostructured nature of the electrodeposit, this thickness is likely an underestimate. We believe this explains why the *operando* spectral response appears to show evidence of saturation, wherein the magnitude of the changes does not increase between cycles 1 and 4, despite the associated plating/stripping currents increasing by at least a factor of three; essentially the ATR surface becomes desensitised to changes after a given thickness of Mg has been deposited, placing a limit on the recommended potential window. Despite the intrinsic sensitivity of this approach to processes at the electrode-electrolyte interface, the analysis is complicated by spectral artifacts associated with the presence of the Pt film, which introduces a potential pitfall to using this method.

CONCLUSIONS

The ATR-IR cell developed in this work has been shown to be suitable for studying Mg electrolytes under operating conditions using different working electrode configurations. It is evident that the two approaches explored probe different aspects of the processes taking place during potential cycling: whereas the Pt gauze primarily gives information on changes to local solution composition, the Pt film is more suited to probing the electrode-electrolyte interface. In this sense, these two methods might be considered to be complementary to each other. However, the Pt film approach is complicated by both the dominant changes in optical transparency of the ATR crystal with Mg plating and the optical artefacts which lead to bipolar/derivative-like line shapes. Hence, caution is recommended in the spectral analysis based on the Pt film configuration. Since the presence of the optical phenomena is strongly related to optical properties of the metal film, there is scope for minimising these issues by optimising the film material, thickness and morphology.

The application of *operando* ATR-IR methodologies to Mg electrolytes has revealed some important considerations in the context of experimental design and data interpretation. Whilst we observed no evidence suggesting chemical degradation of the APC electrolyte studied, both approaches may in principle be suitable for screening the potential stability windows of electrolytes. We note that the use of a Pt working electrode is not representative of conditions in a true working device since the absence of a charge storage material (e.g., an intercalation electrode) affects the nature of the interfacial processes taking place. Hence, more work is underway to extend the application of the methodologies to more complex electrode-electrolyte systems.

ASSOCIATED CONTENT

Supporting Information

The Supporting Information is available free of charge on the ACS Publications website.

Calculation of penetration depth of the IR evanescent wave; Calculation of thickness of plated Mg; ATR-IR spectra of compounds recorded in empty cell without working electrode; SEM-EDX analysis of Mg deposits obtained through plating; ATR-IR spectra as a function of cycle number; Representative contour plot of *operando* ATR-IR data using Pt film configuration. (PDF)

AUTHOR INFORMATION

Corresponding Author

* Andrew J. Wain
Electrochemistry Group
Department of Electromagnetic and Electrochemical Technologies
National Physical Laboratory
Teddington, Middlesex, United Kingdom
Telephone: +44 20 8943 6243
Email: andy.wain@npl.co.uk

Author Contributions

The manuscript was written through contributions of all authors. / All authors have given approval to the final version of the manuscript.

ACKNOWLEDGMENTS

This work was funded by the National Measurement System of the UK Department of Business, Energy and Industrial Strategy and

the EPSRC Impact Accelerator Account (grant code EP/R51178X/1). The authors thank Dr. Jarred Z. Olson for useful comments on the manuscript.

REFERENCES

1. Gregory, T. D.; Hoffman, R. J.; Winterton, R. C., Nonaqueous Electrochemistry of Magnesium: Applications to Energy Storage. *J. Electrochem. Soc.* **1990,** *137* (3), 775-780.
2. Dominko, R.; Bitenc, J.; Berthelot, R.; Gauthier, M.; Pagot, G.; Di Noto, V., Magnesium batteries: Current picture and missing pieces of the puzzle. *J. Power Sources* **2020,** *478*, 229027.
3. You, C.; Wu, X.; Yuan, X.; Chen, Y.; Liu, L.; Zhu, Y.; Fu, L.; Wu, Y.; Guo, Y.-G.; van Ree, T., Advances in rechargeable Mg batteries. *J. Mater. Chem. A* **2020,** *8* (48), 25601-25625.
4. Yoo, H. D.; Shterenberg, I.; Gofer, Y.; Gershinsky, G.; Pour, N.; Aurbach, D., Mg rechargeable batteries: an on-going challenge. *Energy Environ. Sci.* **2013,** *6* (8), 2265-2279.
5. Bonnick, P.; Muldoon, J., A Trip to Oz and a Peak Behind the Curtain of Magnesium Batteries. *Adv. Funct. Mater.* **2020,** *30* (21), 1910510.
6. Attias, R.; Salama, M.; Hirsch, B.; Goffer, Y.; Aurbach, D., Anode-Electrolyte Interfaces in Secondary Magnesium Batteries. *Joule* **2019,** *3* (1), 27-52.
7. Aurbach, D.; Lu, Z.; Schechter, A.; Gofer, Y.; Gizbar, H.; Turgeman, R.; Cohen, Y.; Moshkovich, M.; Levi, E., Prototype systems for rechargeable magnesium batteries. *Nature* **2000,** *407* (6805), 724-727.
8. Mizrahi, O.; Amir, N.; Pollak, E.; Chusid, O.; Marks, V.; Gottlieb, H.; Larush, L.; Zinigrad, E.; Aurbach, D., Electrolyte Solutions with a Wide Electrochemical Window for Rechargeable Magnesium Batteries. *J. Electrochem. Soc.* **2008,** *155* (2), A103.
9. Brouillet, E. V.; Amores, M.; Corr, S. A.; Robertson, S. D., Exploiting cation aggregation in new magnesium amidohaloaluminate electrolytes for magnesium batteries. *Inorg. Chem. Front.* **2020,** *7* (12), 2305-2312.
10. Wang, Z.; Bandyopadhyay, A.; Kumar, H.; Li, M.; Venkatakrishnan, A.; Shenoy, V. B.; Detsi, E., Degradation of magnesium-ion battery anodes by galvanic replacement reaction in all-phenyl complex electrolyte. *J. Energy Storage* **2019,** *23*, 195-201.
11. Brown, S. A.; Cussen, S. A.; Pryke, J. J.; Rae, A.; Robertson, S. D.; Samajdar, R. N.; Marchesini, S.; Wain, A. J., Submitted. *Chem. Commun.* **2022**.
12. Wain, A. J.; O'Connell, M. A., Advances in surface-enhanced vibrational spectroscopy at electrochemical interfaces. *Adv. Phys-X* **2017,** *2* (1), 188-209.
13. Meyer, L.; Saqib, N.; Porter, J., Review—Operando Optical Spectroscopy Studies of Batteries. *J. Electrochem. Soc.* **2021,** *168* (9), 090561.
14. Cowan, A. J.; Hardwick, L. J., Advanced Spectroelectrochemical Techniques to Study Electrode Interfaces Within Lithium-Ion and Lithium-Oxygen Batteries. *Annual Review of Analytical Chemistry* **2019,** *12* (1), 323-346.
15. Wang, Y.; Chen, D., Application of Advanced Vibrational Spectroscopy in Revealing Critical Chemical Processes and Phenomena of Electrochemical Energy Storage and Conversion. *ACS Appl. Mater. Interfaces* **2022,** *14* (20), 23033-23055.
16. Blackburn, T. J.; Tyler, S. M.; Pemberton, J. E., Optical Spectroscopy of Surfaces, Interfaces, and Thin Films. *Analytical Chemistry* **2022,** *94* (2), 515-558.
17. Lim, C.; Kim, J. H.; Chae, Y.; Lee, K.-K.; Kwak, K.; Cho, M., Solvation Structure around Li+ Ions in Organic Carbonate Electrolytes: Spacer-Free Thin Cell IR Spectroscopy. *Analytical Chemistry* **2021,** *93* (37), 12594-12601.
18. Aurbach, D.; Turgeman, R.; Chusid, O.; Gofer, Y., Spectroelectrochemical studies of magnesium deposition by in situ FTIR spectroscopy. *Electrochem. Commun.* **2001,** *3* (5), 252-261.
19. Kuwata, H.; Matsui, M.; Imanishi, N., Passivation Layer Formation of Magnesium Metal Negative Electrodes for Rechargeable Magnesium Batteries. *J. Electrochem. Soc.* **2017,** *164* (13), A3229-A3236.
20. Vizintin, A.; Bitenc, J.; Kopač Lautar, A.; Pirnat, K.; Grdadolnik, J.; Stare, J.; Randon-Vitanova, A.; Dominko, R., Probing electrochemical reactions in organic cathode materials via in operando infrared spectroscopy. *Nat. Commun.* **2018,** *9* (1), 661.
21. Bitenc, J.; Vizintin, A.; Grdadolnik, J.; Dominko, R., Tracking electrochemical reactions inside organic electrodes by operando IR spectroscopy. *Energy Storage Mater.* **2019,** *21*, 347-353.
22. Vizintin, A.; Bitenc, J.; Kopač Lautar, A.; Grdadolnik, J.; Randon Vitanova, A.; Pirnat, K., Redox Mechanisms in Li and Mg Batteries Containing Poly(phenanthrene quinone)/Graphene Cathodes using Operando ATR-IR Spectroscopy. *ChemSusChem* **2020,** *13* (9), 2328-2336.
23. Bančič, T.; Bitenc, J.; Pirnat, K.; Kopač Lautar, A.; Grdadolnik, J.; Randon Vitanova, A.; Dominko, R., Electrochemical performance and redox mechanism of naphthalene-hydrazine diimide polymer as a cathode in magnesium battery. *J. Power Sources* **2018,** *395*, 25-30.
24. Yagi, S.; Tanaka, A.; Ichikawa, Y.; Ichitsubo, T.; Matsubara, E., Electrochemical Stability of Magnesium Battery Current Collectors in a Grignard Reagent-Based Electrolyte. *J. Electrochem. Soc.* **2013,** *160* (3), C83-C88.
25. Eyster, J. M.; Prohofsky, E. W., The normal vibrations of tetrahydrofuran and its deuterated derivatives. *Spectrochim. Acta, Part A* **1974,** *30* (11), 2041-2046.
26. Billes, F.; Böhlig, H.; Ackermann, M.; Kudra, M., A vibrational spectroscopic study on furan and its hydrated derivatives. *Journal of Molecular Structure: THEOCHEM* **2004,** *672* (1), 1-16.
27. Cadioli, B.; Gallinella, E.; Coulombeau, C.; Jobic, H.; Berthier, G., Geometric structure and vibrational spectrum of tetrahydrofuran. *J. Phys. Chem.* **1993,** *97* (30), 7844-7856.
28. Kim, I.-T.; Yamabuki, K.; Sumimoto, M.; Tsutsumi, H.; Morita, M.; Yoshimoto, N., Characteristics of tetrahydrofuran-based electrolytes with magnesium alkoxide additives for rechargeable magnesium batteries. *J. Power Sources* **2016,** *323*, 51-56.
29. Bürgi, T., ATR-IR spectroscopy at the metal–liquid interface: influence of film properties on anomalous band-shape. *Phys. Chem. Chem. Phys.* **2001,** *3* (11), 2124-2130.
30. Zhu, Y.; Uchida, H.; Watanabe, M., Oxidation of Carbon Monoxide at a Platinum Film Electrode Studied by Fourier Transform Infrared Spectroscopy with Attenuated Total Reflection Technique. *Langmuir* **1999,** *15* (25), 8757-8764.
31. Krauth, O.; Fahsold, G.; Magg, N.; Pucci, A., Anomalous infrared transmission of adsorbates on ultrathin metal films: Fano effect near the percolation threshold. *J. Chem. Phys.* **2000,** *113* (15), 6330-6333.
32. Fano, U., Effects of Configuration Interaction on Intensities and Phase Shifts. *Phys. Rev.* **1961,** *124* (6), 1866-1878.
33. Miki, A.; Ye, S.; Osawa, M., Surface-enhanced IR absorption on platinum nanoparticles: an application to real-time monitoring of electrocatalytic reactions. *Chem. Commun.* **2002,** (14), 1500-1501.
34. Liu, T.; Cox, J. T.; Hu, D.; Deng, X.; Hu, J.; Hu, M. Y.; Xiao, J.; Shao, Y.; Tang, K.; Liu, J., A fundamental study on the [(μ-Cl)3Mg2(THF)6]+ dimer electrolytes for rechargeable Mg batteries. *Chem. Commun.* **2015,** *51* (12), 2312-2315.
35. See, K. A.; Chapman, K. W.; Zhu, L.; Wiaderek, K. M.; Borkiewicz, O. J.; Barile, C. J.; Chupas, P. J.; Gewirth, A. A., The Interplay of Al and Mg Speciation in Advanced Mg Battery Electrolyte Solutions. *Journal of the American Chemical Society* **2016,** *138* (1), 328-337.
36. See, K. A.; Liu, Y.-M.; Ha, Y.; Barile, C. J.; Gewirth, A. A., Effect of Concentration on the Electrochemistry and Speciation of the Magnesium Aluminum Chloride Complex Electrolyte Solution. *ACS Appl. Mater. Interfaces* **2017,** *9* (41), 35729-35739.